JGR Atmospheres

RESEARCH ARTICLE
10.1029/2020JD033564

Contrasting Observed Atmospheric Responses to Tropical Sea Surface Temperature Warming Patterns

Anna Mackie[1,5], **Helen E. Brindley**[2,3], **and Paul I. Palmer**[1,4]

[1]School of GeoSciences, University of Edinburgh, Edinburgh, UK, [2]Space and Atmospheric Physics Group, Imperial College London, London, UK, [3]National Centre for Earth Observation, Imperial College London, London, UK, [4]National Centre for Earth Observation, University of Edinburgh, Edinburgh, UK, [5]Now at the University of St Andrews, St Andrews, UK

Key Points:

- We find evidence of contrasting atmospheric responses to relative sea surface temperature warming in regions of strong ascent or descent
- We find that the influence of local warming is limited to the lower troposphere and results in loss of low cloud in areas of strong descent
- Atmospheric response to warming in regions of strong ascent confirms the efficient lofting of warm moist air to the upper troposphere

Supporting Information:

Supporting Information may be found in the online version of this article.

Correspondence to:

A. Mackie,
arm33@st-andrews.ac.uk

Citation:

Mackie, A., Brindley, H. E., & Palmer, P. I. (2021). Contrasting observed atmospheric responses to tropical sea surface temperature warming patterns. *Journal of Geophysical Research: Atmospheres*, *126*, e2020JD033564. https://doi.org/10.1029/2020JD033564

Received 20 JUL 2020
Accepted 10 MAR 2021

Abstract Equilibrium climate sensitivity (ECS) is a theoretical concept which describes the change in global mean surface temperature that results from a sustained doubling of atmospheric CO_2. Current ECS estimates range from ~1.8 to 5.6 K, reflecting uncertainties in climate feedbacks. The sensitivity of the lower (1,000–700 hPa) and upper (500–200 hPa) troposphere to changes in spatial patterns of tropical sea surface temperature (SST) have been proposed by recent model studies as key feedbacks controlling climate sensitivity. We examine empirical evidence for these proposed mechanisms using 14 years of satellite data. We examine the response of temperature and humidity profiles, clouds, and top-of-the-atmosphere radiation to relative warming in tropical ocean regions when there is either strong convection or subsidence. We find warmer SSTs in regions of strong subsidence are coincident with a decrease in lower tropospheric stability (-0.9 ± 0.4 KK^{-1}) and low cloud cover (~-6% K^{-1}). This leads to a warming associated with the weakening in the shortwave cooling effect of clouds (4.2 ± 1.9 Wm^{-2}K^{-1}), broadly consistent with model calculations. In contrast, warmer SSTs in regions of strong convection are coincident with an increase in upper tropospheric humidity ($3.2 \pm 1.5\%$ K^{-1}). In this scenario, the dominant effect is the enhancement of the warming longwave cloud radiative effect (3.8 ± 3.0 Wm^{-2}K^{-1}) from an increase in high cloud cover (~7% K^{-1}), though changes in the net (longwave and shortwave) effect are not statistically significant ($p < 0.003$). Our observational evidence supports the existence of mechanisms linking contrasting atmospheric responses to patterns in SST, mechanisms which have been linked to climate sensitivity.

Plain Language Summary Estimates of how sensitive the Earth's climate is to changes in CO_2 vary between climate models. These models are necessary to explore climate projections, but we need to demonstrate that they can accurately describe the real climate system. Recent model studies hypothesize that the location of surface ocean warming may be key to understanding the atmospheric component of climate sensitivity. We examine observational evidence of the extent to which local tropical ocean warming is able to propagate upwards through the atmosphere. We show that the atmospheric response and associated feedbacks are different in contrasting regions. Future patterns in ocean warming may play a key role in determining future climate.

1. Introduction

Clouds are a major source of uncertainty in physical climate models (Boucher et al., 2013; Soden & Held, 2006; Vial et al., 2013). Low clouds, abundant in the tropical marine regions, have a stronger impact on incoming shortwave radiation than outgoing longwave radiation (OLR) due to their reflectance of solar radiation and their relatively low-temperature contrast with the Earth's surface (Chen et al., 2000; Hartmann et al., 1992; Stephens, 2005). Changes in tropical low cloud cover, and the closely linked tropospheric stability (Klein & Hartmann, 1993; Wood & Bretherton, 2006), therefore strongly influence radiative balance and climate sensitivity (Andrews et al., 2012; Bony & Dufresne, 2005; Ceppi & Gregory, 2017; Qu, Hall, Klein, & Caldwell, 2015; Sherwood et al., 2020; Zelinka et al., 2020). Significant feedbacks in the tropical ocean regions also include the closely linked lapse-rate and water vapor feedbacks, driven by relative changes in temperature and humidity between the lower and upper troposphere. Increasing temperature aloft in isolation leads to increased longwave emission from higher in the troposphere and therefore increased OLR, a (cooling) negative feedback. However, warmer air parcels are associated with higher saturation water

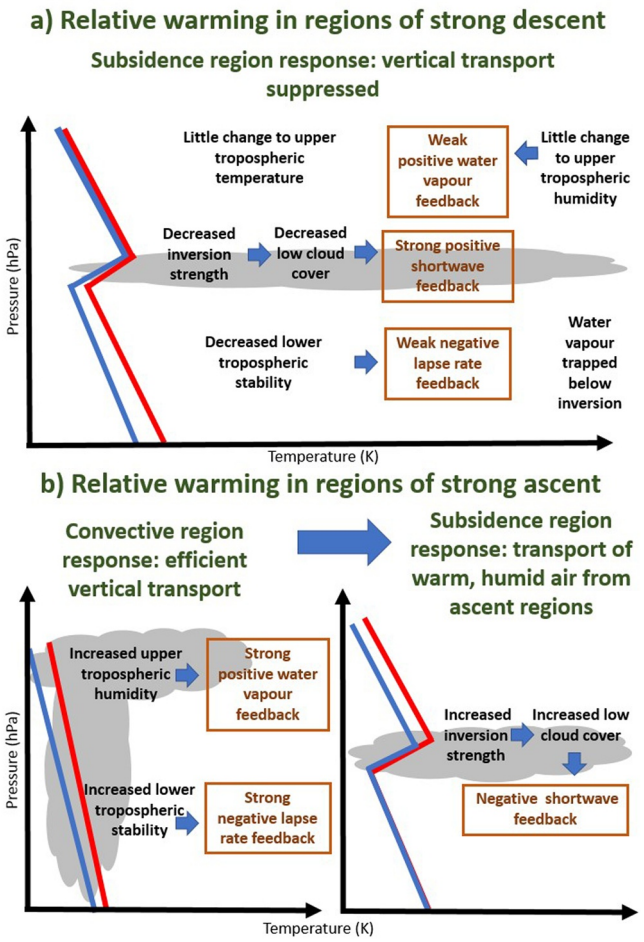

Figure 1. Schematic of hypothesized atmospheric responses to relative sea surface warming of tropical oceans in regions of (a) strong subsidence and (b) strong convection. Blue lines represent initial temperature profiles, red lines represent temperature profiles after relative warming. Response (b) is further split into the responses in convective and subsidence regions. Mechanism as described by Andrews and Webb (2018); Mauritsen (2016); Zhou et al. (2016, 2017).

vapor pressure, which, under a scenario of fixed relative humidity, leads to a decrease in OLR, or a (warming) positive feedback (Allan et al., 1999; Held & Soden, 2000). These changes in OLR are most sensitive to humidity perturbations in the upper troposphere (Brindley & Harries, 1998).

Here, we use data from the NASA *Aqua* satellite from 2002 to 2016, including temperature and humidity profiles, cloud fraction, and top-of-the-atmosphere (TOA) broadband radiation flux, to evaluate evidence of a hypothesized mechanism which links patterns in sea surface temperature (SST) to lower tropospheric stability (LTS), upper tropospheric humidity (UTH), and low cloud cover (Figure 1, as described by Andrews & Webb, 2018; Ceppi & Gregory, 2017; Mauritsen, 2016; Zhou et al., 2016, 2017). A key determining factor is the relative warming of SSTs in either convective or subsidence regions of the tropical ocean. In both scenarios, an important step in the mechanism is the connection between the lower and upper troposphere and the extent to which relative warming at the surface is able to propagate up and influence the free troposphere.

In this hypothesis, if the SST warming is concentrated in subsidence regions, much of the warming is effectively "trapped" under the temperature inversion which caps the boundary layer at around 700 hPa (Andrews & Webb, 2018; Zhou et al., 2016) leading to warmer, moister air in the lower troposphere, while humidity above the inversion remains low (Figure 1a). Warmer, moister air at the top of the boundary layer results in decreased inversion strength and reduced cloud cover (McCoy et al., 2017; Wood, 2012; Wood & Bretherton, 2006). The relative warming of the surface compared to the top of the boundary layer reduces LTS, drawing in warm, dry air from above the inversion, which further reduces low cloud cover resulting in a strong shortwave cloud feedback (Ceppi & Gregory, 2017; Fasullo & Trenberth, 2012). As the lower troposphere (below the inversion at 700 hPa) warms and becomes less stable, OLR at the TOA increases due to increased surface temperature and less absorption from low clouds. Little warming above the inversion results in the negative lapse-rate feedback being weak (Figure 1a). The small increase in UTH also leads to a weak positive water vapor feedback (Ceppi & Gregory, 2017). The net effect is dominated by the shortwave cloud feedback which leads to a more positive cloud feedback and greater implied equilibrium climate sensitivity (ECS) than if SST warming is concentrated in ascent regions (Andrews & Webb, 2018).

Conversely, it is hypothesized that if surface warming is focused in tropical convective regions, warm, moist air is efficiently transported above 700 hPa, leading to similar or even greater warming in the mid-troposphere than at the surface. The negative lapse-rate and positive water vapor feedbacks counteract each other, reducing the overall feedback in the convective regions to have either a weak positive or weak negative sign (Figure 1b). However, the movement of warm, moist air aloft also affects stability in subsidence regions, as lateral transport leads to stronger subsidence, and consequently increased stability and low cloud cover, in the subsidence regions. This increase in low cloud cover in subsidence regions may offset the local decrease in low cloud cover in convective regions as they warm, leading to a lower implied ECS than if warming were concentrated in descent regions (Andrews & Webb, 2018).

Model fidelity relies on accurate descriptions of the underlying climate physics, including many emergent features that are difficult to describe explicitly. Therefore, observational evidence is needed, where possible, to evaluate mechanisms which have been proposed based on model experiments. However, a number of studies have highlighted the difficulties in estimating climate sensitivity from observational energy budget records due to time-varying feedbacks, for example the effects of SST warming patterns described above

(Andrews et al., 2015; Armour, 2017; Zhou et al., 2016). Using local observations and processes, for example in the tropics, to infer wider climate feedbacks and sensitivity is difficult, not least due to complex, and potentially competing nonlocal effects (Lindzen et al., 2001; Mauritsen & Stevens, 2015; Pierrehumbert, 1995; Ramanathan & Collins, 1991; Trenberth et al., 2010). For example, recent work by Bloch-Johnson et al. (2020) finds, using a multiple regression method on coupled GCMs, that local positive feedbacks in the tropics are balanced by associated nonlocal feedbacks.

Despite these difficulties, the benefits of observational evidence for process studies are clear. Observational studies have been used to establish evidence linking low cloud cover with surface warming and lower tropical stability, and an associated reduction in TOA shortwave radiation (Brient & Schneider, 2016; McCoy et al., 2017; Myers & Norris, 2016; Qu et al., 2014; Qu, Hall, Klein, & DeAngelis, 2015; Scott et al., 2020), but while they generally support a positive feedback, the implications for climate sensitivity are unclear (Bretherton, 2015; Klein et al., 2017; Sherwood et al., 2014). A number of recent studies draw on some observational evidence of the SST pattern effect through the proposed mechanism discussed above. For example, Fueglistaler (2019) establishes some evidence for the impact of the SST pattern effect by demonstrating the coupling between SSTs of the warmest parts of the tropical ocean and tropospheric boundary layer capping strength and shortwave cloud radiative effect (CRE) over the whole tropical ocean. Furthermore, Ceppi and Gregory (2017) present global qualitative observational evidence linking the spatial patterns in SST, LTS, and TOA radiation fluxes. Here, we examine in more detail the extent to which temperature and humidity increases in the lower troposphere are coupled to the upper troposphere, the initial step in the mechanism described above using co-incident, independent observations from the *Aqua* satellite. By utilizing both the short- and longwave part of the spectrum, including separating the longwave window and nonwindow effects, we interpret TOA radiation flux changes with respect to these atmospheric and cloud changes.

2. Materials and Methods

2.1. Satellite Data and Meteorological Analyses

We use monthly mean, co-incident measurements of TOA radiation, cloud, temperature, and humidity from instruments aboard the NASA Aqua satellite, inclusively from October 2002 to September 2016. Aqua is in a sun-synchronous orbit with local equator crossing times of 0130 and 1330. We use broadband all- and clear-sky TOA reflected shortwave radiation (RSR, 0.3–5 μm), OLR (-5–200 μm) and window region (WN, 8–12 μm) radiation flux from the Clouds and Earth's Radiant Energy System (CERES) instrument. We use Single Scanner Footprint data, at a one degree spatial resolution (SSF1deg), Edition 4A (Doelling et al., 2013; Loeb et al., 2018). We also use SSF1deg cloud fraction data that are derived from the proportion of clear and cloudy pixels as identified by the Moderate Resolution Imaging Spectroradiometer (MODIS). These data are split into low (surface–700 mb), mid-low (700–500 mb), mid-high (500–300 mb), high (300–70 mb), and total (surface–70 mb) cloud fractions, with up to two cloud layers possible. We use Level 2 cloud-cleared surface skin temperature and atmospheric temperature and humidity profiles at 1,000, 850, 700, 600, 500, 400, 300, 200 and 150 hPa from the Atmospheric Infrared Sounder (AIRS)/Advanced Microwave Sounding Unit (Aumann et al., 2003), version 6. We are only using ocean data, so we hereinafter refer to skin temperature as SST. Finally, we use vertical velocity at 500 hPa from the European Center for Medium-Range Weather Forecasts reanalysis ERA-Interim (ERA-I) to identify regions of strong ascent and descent, as detailed below. We use all ocean data at $1° \times 1°$ resolution, between 30°S and 30°N. We use longwave (LW), shortwave (SW), net (LW plus SW), and window region (WN) fluxes in our analyses, and take downwelling as positive for all TOA radiation fluxes. This results in positive values indicating a warming of the Earth-atmosphere system.

We acknowledge differences in definitions adopted by CERES SSF1deg clear-sky radiation fluxes and AIRS cloud-cleared profiles. AIRS uses clear column radiances in adjacent fields of view to infer cloud-cleared radiances in cloudy scenes with two key assumptions. First, it assumes that a particular type of cloud always has the same radiative properties which scale with cloud amount. Second, it assumes that the temperature and humidity profiles do not differ between cloudy and clear portions of a scene (Susskind et al., 2003). This cloud-clearing method may introduce cold and dry biases, particularly where there are thick clouds (Wong et al., 2015). In comparison, CERES SSF1deg uses MODIS to identify clear-sky pixels (~1 km), with a CERES footprint (~20 km) categorized as clear-sky if 99% of MODIS pixels are cloud free (Minnis

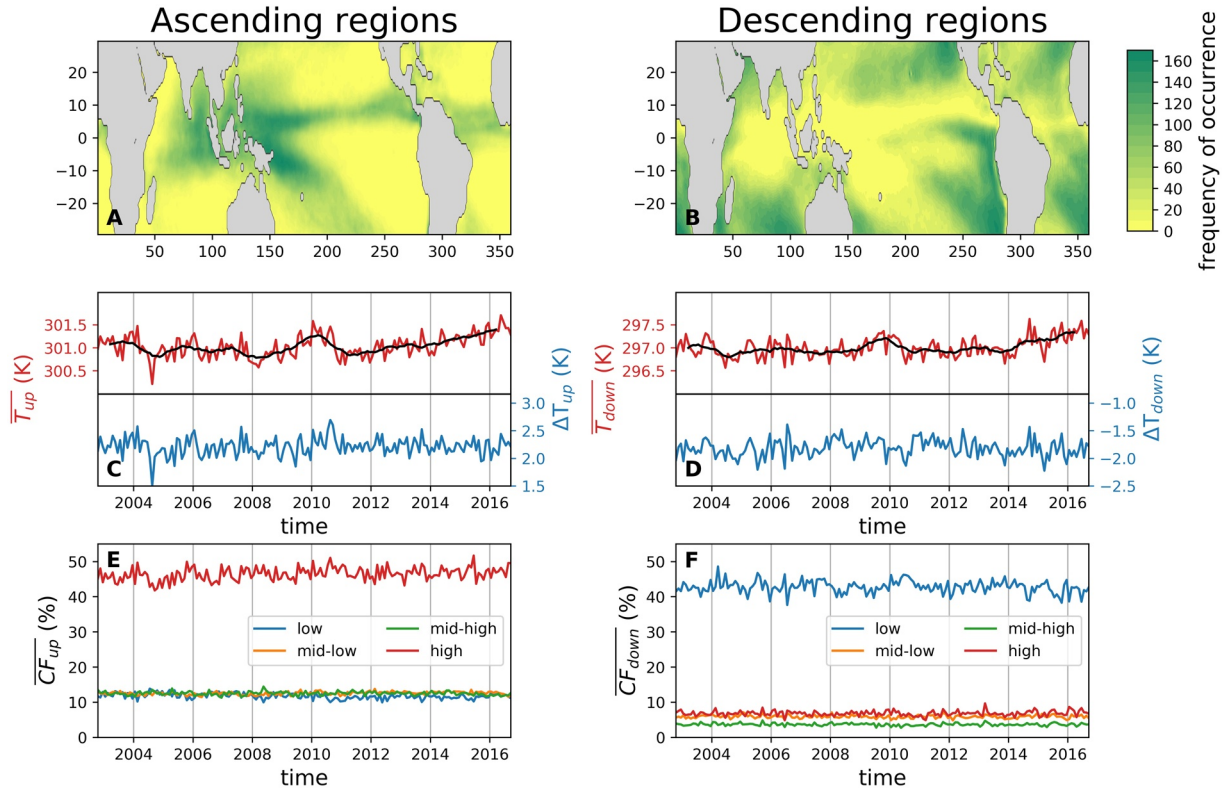

Figure 2. Spatial frequency of grid points selected as (a) ascending points and (b) descending points. Deseasonalized mean temperature (red lines) in (c) ascending ($\overline{T_{up}}$) and (d) descending ($\overline{T_{down}}$) regions. The corresponding 12 months running means are shown as black lines. Deseasonalized temperature relative to tropical ocean mean for (c) ascending (ΔT_{up}) and (d) descending (ΔT_{down}) regions is defined as the $\overline{T_{up}}$ and $\overline{T_{down}}$ minus the mean temperature of tropical oceans (see Section 2). Deseasonalized mean cloud fraction, split into total, low, mid-low, mid-high, and high altitudes (see Section 2), for (e) ascending and (f) descending regions.

et al., 2011). This results in some missing data in clear-sky radiation fluxes. While we take the mean of day and night overpass measurements to obtain the AIRS monthly means, SSF1deg is produced by interpolating Aqua measurements at overpass times into hourly timesteps and then the mean is taken over these hourly intervals (Doelling et al., 2013). However, we use large spatial averages and monthly resolution data, which should minimize this effect. Using all-sky and clear-sky OLR from AIRS does not significantly alter the analysis, suggesting that the different processing methods do not have a large impact on our results.

2.2. Mean Meteorological Data Over Tropical Strongly Ascending and Descending Regions

We define regions of the tropical ocean with strong ascent and descent using vertical velocity at 500 hPa ($\omega 500$), following Bony et al. (2004) and Zhou et al. (2016). These regions are defined dynamically each month, with grid points selected on a month-by-month basis. Strongly ascending and descending regions at a time t, latitude θ and longitude λ are determined using the following criterion: if the absolute value of $\omega 500(t, \theta, \lambda)$ is greater than the median value of $\omega 500$ over the tropical oceans for either descending ($\omega 500(t, \theta, \lambda) > 0$) or ascending ($\omega 500(t, \theta, \lambda) < 0$) regions. This method effectively identifies four regimes at any one time: strong ascent, weak ascent, weak descent, and strong descent, with the boundaries between strong and weak determined by the median value for that month. The frequency with which points are selected into strongly ascending and descending regions are shown in Figures 2a and 2b. For clarity, we henceforth refer to these strongly ascending and descending regions as simply ascending and descending regions, and discard the weaker ascending and descending regions from the majority of our analysis. Our focus on strongly ascending and descending regions arises from the wish to isolate relationships in the limited observational data, and these may be clearer when using more extreme cases. However, our use of the median

in defining "strong" is motivated in keeping this definition broad enough to select coherent geographical regions (Figures 2a and 2b).

We determine the corresponding differences in SST anomalies at time t by calculating the deseasonalized mean temperature associated with ascending and descending regions ($\overline{T_{up}}$, $\overline{T_{down}}$) and then subtracting the deseasonalized mean temperature over tropical oceans. The result is the temperature anomalies associated with the strongly ascending ΔT_{up} and descending ΔT_{down} regions. By selecting points using $\omega 500$ we account for periodic shifts in geographical areas of convection and subsidence due to large-scale dynamics, in particular the El Niño Southern Oscillation, a leading mode in the temperature of the warmest parts of the tropical ocean (Fueglistaler, 2019).

One potential difficulty with this method is that the changes in ΔT_{up} and ΔT_{down} are influenced both by local changes and also changes in the tropical ocean mean. However, the lack of statistically significant correlation between the tropical ocean mean temperature $\overline{T_{trp}}$ and ΔT_{up} or ΔT_{down} suggests that the latter are not solely driven by the mean tropical ocean temperatures. We discuss this further in the Section 4.

To explore the response of the atmosphere in strongly ascending or descending regions to relative surface warming, we linearly correlate temperature, humidity, and radiation data that have been subsetted and averaged using the method described above. In general, variables associated with the mean over strong ascending and descending regions are denoted by an overline and the subscripts *up* and *down*, respectively. For example, the correlation between ΔT_{up} and $\overline{LW_{up}}$ examines the co-variability of the longwave radiation at the top of the atmosphere in ascending regions in response to relative warming in those regions. We perform similar analysis using two derived variables: UTH, the mean relative humidity between 200 and 500 hPa, inclusively; and LTS, the difference in atmospheric potential temperature between 700 and 1,000 hPa. We deseasonalize the monthly data by removing the difference between the climatological mean of that month from the series mean.

We use the standard error of the mean to describe the uncertainty of our derived mean ascending and descending values and propagate this error in subsequent calculations of the variable. Because our mean variables represent large geographical areas, the standard deviation is expected to be larger than measurement random errors that scale with the square-root of number of independent observations. We use a least squares linear regression, with the uncertainty in each point equal to $\sqrt{\epsilon_x^2 + \epsilon_y^2}$, where ϵ_x and ϵ_y are the uncertainties in the variables being regressed. We use the Pearson correlation coefficient r and p-values from the fit to indicate the strength and significance of the relationship. We assume values of $p < 0.003$ to be statistically significant.

3. Results

3.1. Data over Ascending and Descending Regions

Figures 2a and 2b show maps of the number of times grid points were selected for the ascending and descending regions (Section 2). Ascending grid points are located in areas of deep convection, especially over the West Pacific warm pool, as expected; these represent 19% of all points. Descending grid points are mainly located near coastal regions that are associated with extensive stratiform cloud decks (e.g., west coast of the Americas), and the sub-tropics; these points represent 31% of all data considered.

We find no significant trends in deseasonalized mean SST for either ascending regions ($\overline{T_{up}}$, Figure 2c) or descending regions ($\overline{T_{down}}$, Figure 2d). Furthermore, the amplitude of variability in both regions is similar at < 1 K. Variations in the mean SST in ascending and descending regions relative to the whole tropical ocean (ΔT_{up}, ΔT_{down}, Section 2) show a similar amplitude ($\sim$1 K) and high month-to-month variability. We do not find statistically significant linear correlations between $\Delta T_{up/down}$ and $\overline{\omega 500_{up/down}}$ (not shown).

As expected for regions of deep convection, high cloud dominates in the ascending regions (Figure 2e), with deseasonalized high cloud fraction typically 40%–50%. Low and mid cloud fractions are lower at $\sim$10%,

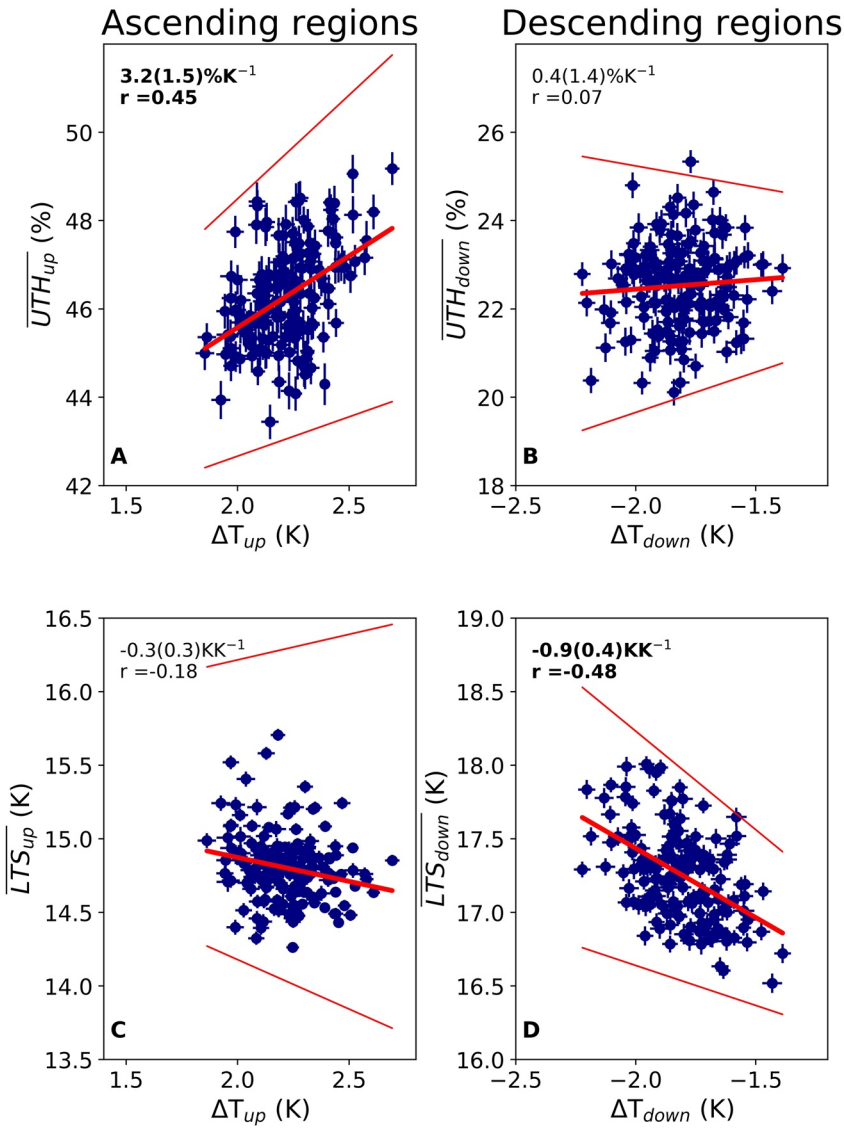

Figure 3. Scatterplots of upper tropospheric humidity (UTH) and relative warming ΔT in (a) ascending and (b) descending regions; and lower tropospheric stability (LTS) and relative warming ΔT in (c) ascending and (d) descending regions. All data have deseaonalized. Error bars are reported as standard errors on the mean (see Section 2). The least squares linear fit is shown as a bold red line, with the associated error of the slope (three standard deviations) shown as thin red lines. Inset text reports the fitted regression slope, with uncertainty (three standard deviations) in round brackets, and the Pearson correlation coefficient r. Text is bold if they are statistically significant ($p < 0.003$).

though this may be affected by high cloud masking. In areas of subsiding air (Figure 2f) we see that low clouds dominate, as expected, with low cloud fractions of 40%–50%, and other higher altitude cloud fractions of < 10%.

3.2. Changes in Upper Tropospheric Humidity and Lower Tropospheric Stability with Relative Surface Warming

Figure 3 shows how UTH and LTS change with relative warming over ascending and descending regions.

Figure 3a shows that over ascending regions, there is a statistically significant increase in $\overline{UTH_{up}}$ with increasing values of ΔT_{up} (3.2 ± 1.5% K^{-1}). This is consistent with efficient vertical transport of warm, moist

air from the surface to the mid-upper troposphere, as hypothesized by the mechanisms discussed in Section 1. Figure 3c shows that there is no statistically significant change in the LTS in this region, similarly consistent with the proposed mechanisms, which predict that an increase in relative SST (ΔT_{up}) would be accompanied by a similar increase in temperature aloft (700 hPa) as at the near-surface (1,000 hPa) (Figure 1).

Figures 3b and 3d show similar analyses for the descending regions, where relative warming (ΔT_{down}) is hypothesized (Andrews & Webb, 2018) to be trapped beneath a low level inversion (Figure 1). We find a statistically significant decrease in $\overline{LTS_{down}}$ (Figure 3d) with increasing relative surface warming ΔT_{down} (-0.9 ± 0.4 KK^{-1}), as expected. We do not find a statistically significant change in $\overline{UTH_{down}}$ with increasing surface warming ΔT_{down} (Figure 3b) supporting the idea of a temperature inversion suppressing vertical transport.

While the above analysis largely supports the proposed mechanisms, we explore the contrasting scenarios in more detail by further examining coincident changes in temperature, humidity, cloud coverage, and radiation fluxes.

3.3. Further Characterization of the Atmospheric Responses to Relative Surface Warming

We present our results in two ways for ascending and descending regions. First, we report the slope, Pearson correlation coefficients r, and statistical significance of linear regressions between relative surface warming ΔT and atmospheric temperature $\overline{temp}$, the natural logarithm of specific humidity $\overline{ln(q)}$, and relative humidity $\overline{rh}$ at different pressure levels from 1,000 to 200 hPa. This analysis provides us with insight about the vertical influence of ΔT. We examine $\overline{ln(q)}$ rather than $\overline{q}$ as radiation is proportional to the logarithm of specific humidity (Soden & Bretherton, 1993). Second, we examine changes to the TOA broadband radiation fluxes associated with these atmospheric and surface changes. We show how net (shortwave plus longwave), shortwave, longwave, window-region, and nonwindow region fluxes, separated into all-sky, clear-sky and CRE (all-sky minus clear-sky), are related to relative surface warming ΔT over ascending and descending regions. Separating these radiation fluxes in this way provides us with insight into the responsible physical processes. We first examine the ascending region (subscript *up*), before the descending region (subscript *down*). Over ascending regions, we find statistically significant warming between 1,000 and 300 hPa of up to ~1.2 KK^{-1} (Figure 4a), with the strongest warming near the surface. The rate of warming is approximately constant up to 300 hPa, above which it decreases with altitude, providing further evidence of the efficient convective heat transfer through the troposphere. We also find a statistically significant increase in $\overline{ln(q_{up})}$ from 1,000 to 150 hPa (Figure 4b), with an increase of ~0.1 ln(gKg)$^{-1}$ K^{-1} at 1,000 hPa, which increases approximately linearly with altitude up to a maximum at 500 hPa of ~0.2 ln(gKg)$^{-1}$ K^{-1}. These combined changes in temperature and specific humidity result in a statistically significant increase in relative humidity with ΔT_{up} above 850 hPa, with the largest increases of ~5% K^{-1} between 600 and 400 hPa (Figure 4c). This analysis demonstrates that the increase in UTH as a function of ΔT_{up} (Figure 3a) is due to the dominant role of the increase in UTH over that in temperature. Figure 4d shows that there are significant changes in total, low and high cloud fraction with changes in ΔT_{up} of ~3% K^{-1}, −2.5% K^{-1} and 7% K^{-1}, respectively. An increase in high cloud fraction with an increase ΔT_{up} is consistent with an increase in rising, warm air that results in an increase in clouds rising to, or forming at, higher altitudes. The increase in high cloud, however, may be masking the detection of low cloud.

Continuing our examination of the ascending regions, Figures 5d–5f show there are no significant correlations between ΔT_{up} and all-sky, clear-sky, or CRE shortwave radiation ($\overline{SW_{up}}$) fluxes. For longwave radiation fluxes, we find a statistically significant increase in all-sky $\overline{LW_{up}}$ fluxes (4.8 ± 3.8 Wm^{-2} K^{-1}, Figure 5g), driven by clouds. The increase in the longwave warming effect of clouds with increasing ΔT_{up} (3.8 ± 3.0 Wm^{-2}K^{-1}, Figure 5i) is consistent with our hypothesis of enhanced convection with ΔT_{up}, which results in an observed increase in high cloud fraction and a reduction in longwave emission to space. Enhanced high cloud fraction also enhances reflected shortwave radiation, and while these effects are not statistically significant using our criterion, we see a decrease of -3.7 ± 4.7 Wm^{-2}K^{-1} in all-sky SW fluxes (Figure 5d),

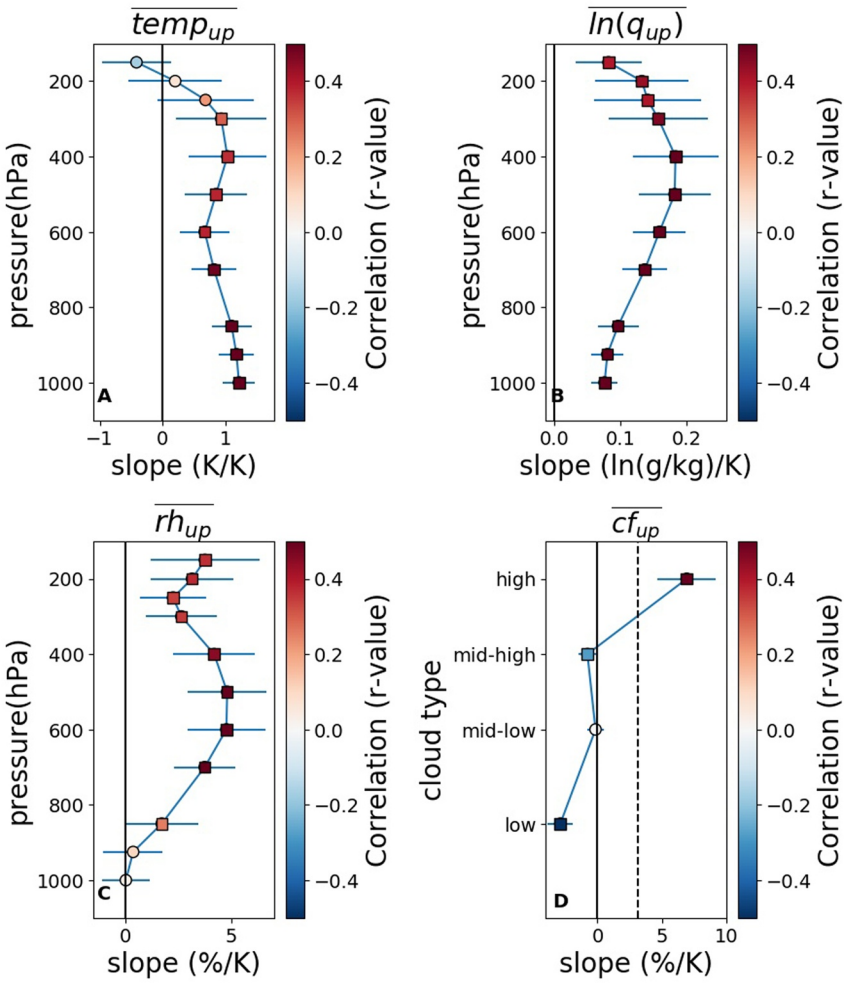

Figure 4. The linear regression slope between ΔT_{up} and (a) atmospheric temperature, (b) the natural logarithm of specific humidity, and (c) relative humidity as a function of pressure (hPa). Colors of the filled symbols denote the magnitude of the Pearson correlation coefficient. Horizontal lines denote three standard deviations. Squares denote statistical significance ($p < 0.003$), while circles denote a statistically insignificant correlation. Panel (d) reports the same analysis between ΔT_{up} and low, mid-low, mid-high, and high cloud fraction, with total cloud fraction marked with a vertical dashed line. All data have been deseasonalized.

driven by an enhanced shortwave cooling effect from the increased high cloud (-2.0 ± 4.3 Wm^{-2}K^{-1}, Figure 5f). While changes in the net (longwave plus shortwave) effect, $\overline{Net_{up}}$, are not statistically significant in the all-sky, clear-sky, or CRE (Figures 5a–5c), we see that there is an increase in the net CRE, corresponding to a weakening of the net cooling effect of clouds (2.1 ± 2.3 Wm^{-2}K^{-1}, Figure 5c). This is due to the enhancement of the longwave warming effect of the high clouds (Figure 5i) being stronger than the enhancement of the cooling effect in the shortwave (Figure 5f). This incomplete compensation could be due to increases in cloud top height with ΔT_{up}, though we leave examination of this for future study.

The correlations between variations in ΔT_{up} and window $\overline{WN_{up}}$ and nonwindow $\overline{(LW - WN)_{up}}$ longwave fluxes give more insight into the underlying physical processes. The window region is sensitive to surface conditions and the presence of clouds, while nonwindow longwave fluxes are more affected by atmospheric and cloud changes in the mid-upper troposphere. We find that the changes in $\overline{LW_{up}}$ (Figure 5g) result primarily from nonwindow effects (3.3 ± 2.3 Wm^{-2}K^{-1}, Figure 6d): changes in all-sky window longwave fluxes (Figure 6a) are not statistically significant, and result from the cancellation of the statistically significant decrease in clear-sky flux (-0.9 ± 0.5 Wm^{-2}K^{-1}, Figure 6b) with the increase in CRE (1.5 ± 1.4 Wm^{-2}K^{-1},

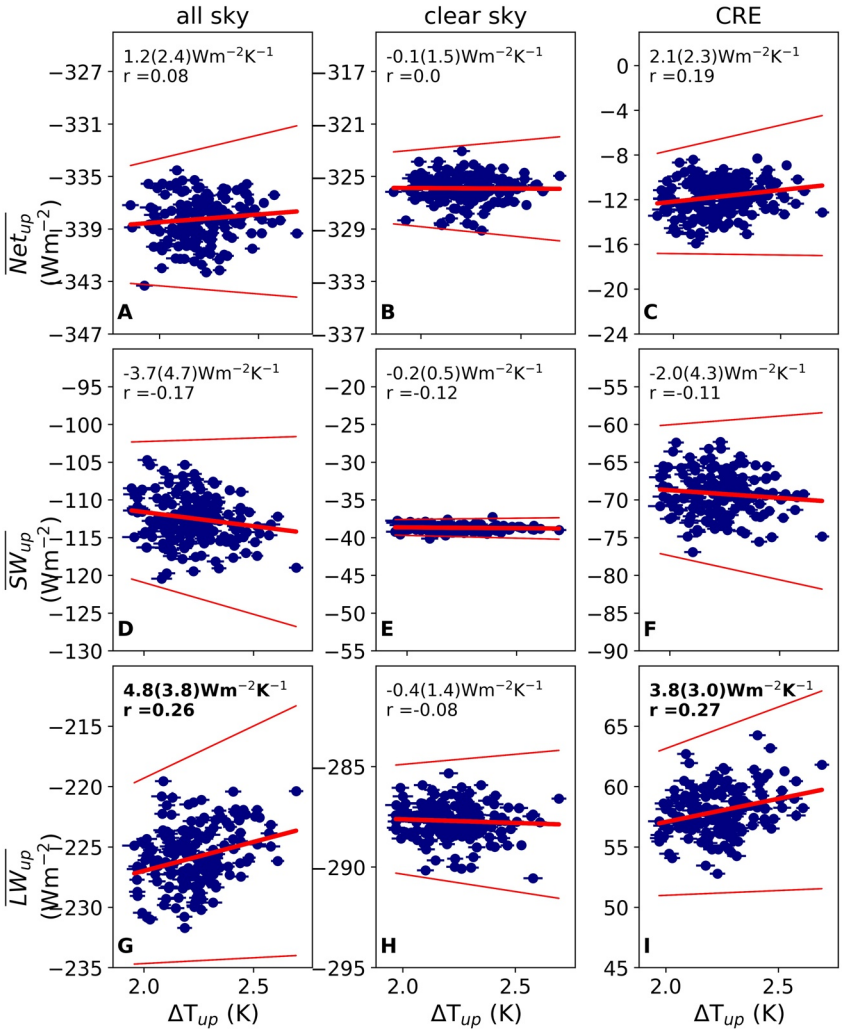

Figure 5. Scatterpots of ΔT_{up} and top-of-atmosphere broadband radiation fluxes over ascending regions. The fluxes are split between (columns) all-sky, clear-sky, cloud radiative effect (CRE = all-sky minus clear-sky), and between (rows) net (shortwave plus longwave) radiation, shortwave radiation (SW), and longwave radiation (LW). The positive direction for all fluxes is downwards, and positive numbers indicate a warming effect. All data have been deseasonalized. A significantly outlying point has been removed. Radiation flux data are from CERES SSF1deg and SST data are from AIRS (see Section 2.2). The least squares linear fit is shown as a bold red line, and three standard deviations on the slope are shown as thin red lines. Inset text reports the fitted regression slope, with uncertainty in round brackets, and the Pearson correlation coefficient *r*. Text is bold if they are statistically significant ($p < 0.003$).

Figure 6c). We link the former of these changes to surface warming and the second to the increased high cloud fraction. In contrast, the changes in nonwindow longwave fluxes are largely due to a statistically significant increase in the CRE (2.2 ± 1.9 Wm^{-2}K^{-1}, Figure 6f).We now begin our analysis of the descending region. In these regions, the relationship between changes in $\overline{temp_{down}}$ and ΔT_{down} ranges from ~1.1 KK^{-1} at 1,000 hPa to 0.6 KK^{-1} at 850 hPa (Figure 7a), a region over which the correlations between the two variables are statistically significant. This supports the hypothesis that an inversion is restricting the transport of warm, moist air to the upper troposphere (Figure 1), with no statistically significant temperature changes above 700 hPa. We find significant increases in specific humidity ($\overline{ln(q_{down})}$) are limited to 600 hPa and lower altitudes (Figure 7b). The rapid decrease above 600 hPa could also be consistent with moisture being trapped by the inversion, though statistically significant increases in moisture are observed at 700–600 hPa, where temperature increases are not significant. The combined changes in atmospheric temperature and specific humidity over descending regions result in an increase in relative humidity between 850 and

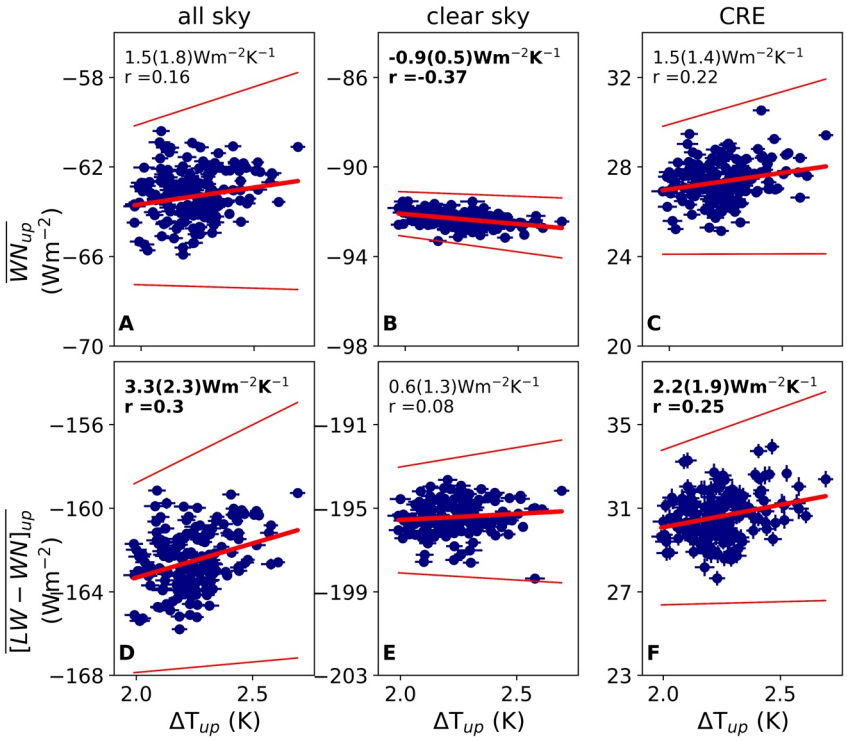

Figure 6. As Figure 5, but for window (WN) and nonwindow (LW–WN) radiation fluxes.

600 hPa (Figure 7c), approximately where we might expect an inversion. These findings are consistent with the lack of significant change in UTH (Figure 3b) and decrease in LTS (Figure 3d) with increasing ΔT_{down}. Consistent with the decrease in LTS, we see a strong decrease ($\sim 6\%K^{-1}$) in low cloud cover in descending regions with ΔT_{down} (Figure 7d). At higher levels we see smaller, statistically significant increases in mid-low cloud fraction, though the response of the total cloud fraction is driven by the reduction in low cloud fraction (Figure 7d) and is therefore negative ($\sim -5\%\ K^{-1}$).

We find a strong response in the $\overline{SW_{down}}$ fluxes to changes in ΔT_{down} (Figures 8d–8f). The increase in all-sky $\overline{SW_{down}}$ fluxes with increasing ΔT_{down} of $3.9 \pm 2.3\ Wm^{-2}K^{-1}$, indicates enhanced absorbed shortwave radiation as local SSTs increase. We see that this effect is driven by a weakening of the shortwave cooling effect of clouds ($4.2 \pm 1.9\ Wm^{-2}K^{-1}$, Figure 8f) consistent with the decrease in low cloud fraction. There are no statistically significant correlations between ΔT_{down} and all-sky, clear-sky or CRE $\overline{LW_{down}}$ fluxes (Figures 8g and 8i), though there is decrease in the longwave CRE of $-1.1 \pm 1.3\ Wm^{-2}K^{-1}$ (Figure 8i). This decrease in the longwave warming effect of clouds is also consistent with the reduction in low cloud cover. The strong weakening in the cooling shortwave effect dominates over this reduction in the longwave warming effect in $\overline{Net_{down}}$ ($2.5 \pm 2.3\ Wm^{-2}K^{-1}$ (Figure 8a). This is indicative of a net warming with increased local SST, driven by CREs ($3.0 \pm 1.8\ Wm^{-2}K^{-1}$, Figure 8c).

Examination of window and nonwindow effects shows statistically significant decreases in the window region fluxes with local SST warming (Figures 9a–9c). We interpret the decrease in clear-sky window flux ($-0.7 \pm 0.4\ Wm^{-2}K^{-1}$, Figure 8b), corresponding to an increase in window region radiation to space, as resulting from surface warming, and the decrease in the CRE ($-0.6 \pm 0.5\ Wm^{-2}K^{-1}$, Figure 8c) as from the decrease in low cloud fraction. In contrast, there are no statistically significant changes ΔT_{down} in the nonwindow region, supporting the hypothesis that the influence of local SST warming does not reach the mid-troposphere.

Finally, we briefly examine evidence for the remote effect of increasing SSTs in strongly ascending regions (ΔT_{up}) on regions of descent and also on the radiation budget of the whole tropical ocean. To do this, we

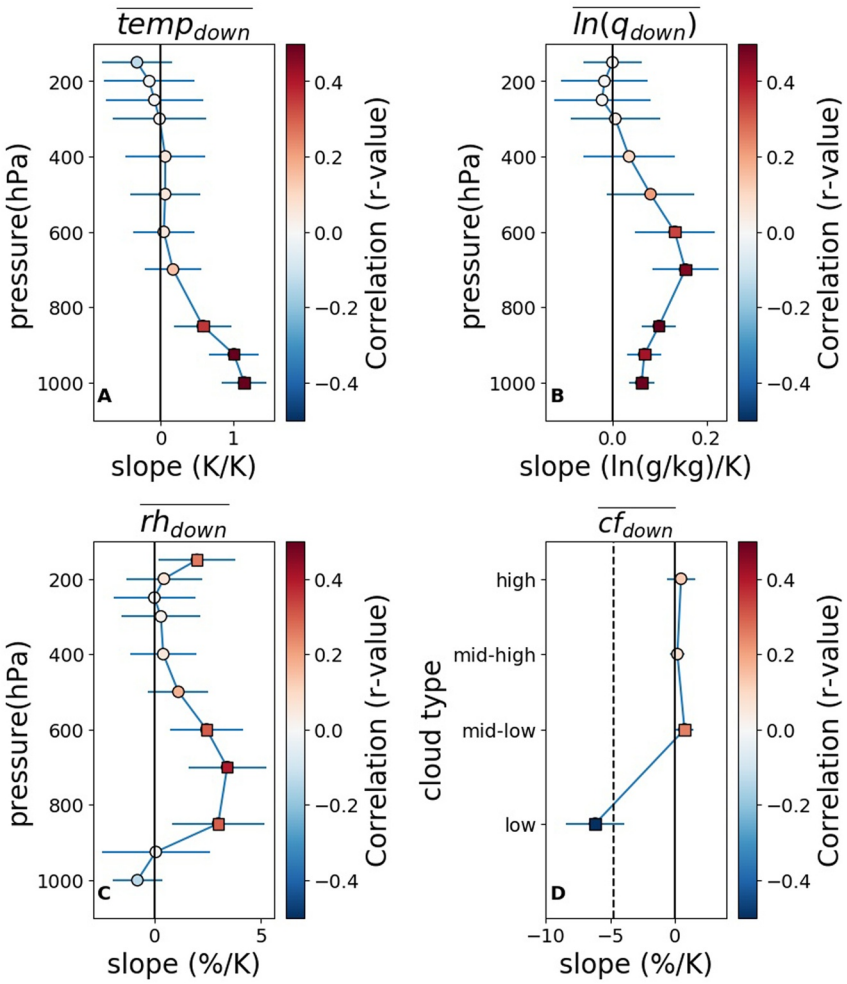

Figure 7. As Figure 4 but for descending regions.

examine the correlation between ΔT_{up} and the mean net, shortwave and longwave CREs over the whole tropical ocean (Figure 10a, 10c, and 10e), as well as the mean CRE over all descending oceanic grid points (Figure 10b, 10d, and 10f). We highlight that in this final section, "all descending" refers to all tropical ocean points with descending motion at 500 hPa in a given month, in contrast to our previous definition. This change reflects that, from studies such as that by Andrews and Webb (Figure 2018) and others, we expect the remote effects of increasing SST in convective regions to affect regions of subsidence in general, and not be restricted to those of strong subsidence.

We find no significant correlations in CRE with ΔT_{up} with whole tropical ocean means, suggesting that, at this timescale, increases in the SST in convective regions are unable to impact the radiation budget over the whole tropical ocean through cloud processes. However, we note that such relationships may be detectable at longer timescales: for example, Fueglistaler (2019) found, using a low-pass filter of a 6 months running mean, significant correlations between the SST of the warmest regions with the tropical mean shortwave CRE. We do, however, find a statistically significant decrease of -1.8 ± 1.3 Wm^{-2} in shortwave CRE in all descending regions with ΔT_{up} (Figure 10d), consistent with the increase in low cloud hypothesized by Andrews and Webb (2018) and outlined in Section 1, though this does not lead to a statistically significant decrease in the net CRE (Figure 10b).

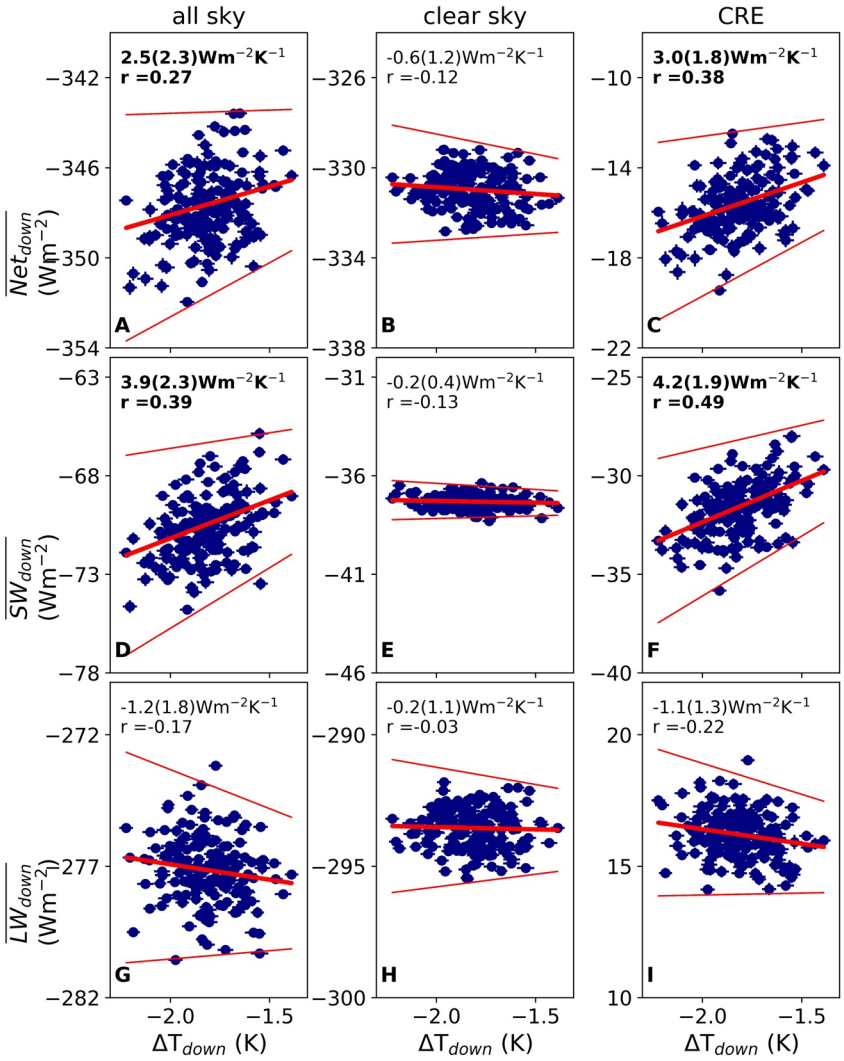

Figure 8. As Figure 5 but for descending regions.

4. Summary and Discussion

SST warming in the past decades has been concentrated in the tropical marine ascent regions and has been linked to dampened warming through an associated increase of low cloud in subsidence regions (Zhou et al., 2016). A key step in this process is the lofting of warm, moist air into the free troposphere in the ascent regions as they preferentially warm. We show that under this scenario, while the largest local temperature changes are realized near the surface, the LTS does not significantly change with local warming. We also see changes in upper tropospheric temperature and humidity that lead to a marked increase in UTH, consistent with model hypothesis as described in Andrews and Webb (2018). Moreover, our evidence suggests that the accompanying increase in high cloud results in a marked increase in the warming longwave CRE which dominates the net local TOA cloud radiative response, though these changes are not statistically significant.

Under the scenario of relative warming in subsidence regions, the presence of humidity increases above ~700 hPa suggests that the inversion does not completely suppress vertical transport, though in general temperature and the largest humidity increases are concentrated within the lowest levels of the troposphere. This combination of temperature and humidity changes leads to increases in relative humidity in the 850–600 hPa band, where we expect our inversion to be. Consistent with past work (Ceppi & Gregory, 2017; McCoy et al., 2017), we find strong evidence that warming in subsiding regions reduces local tropospheric stability, and results in a strong decrease in low cloud cover and an associated decrease in reflected

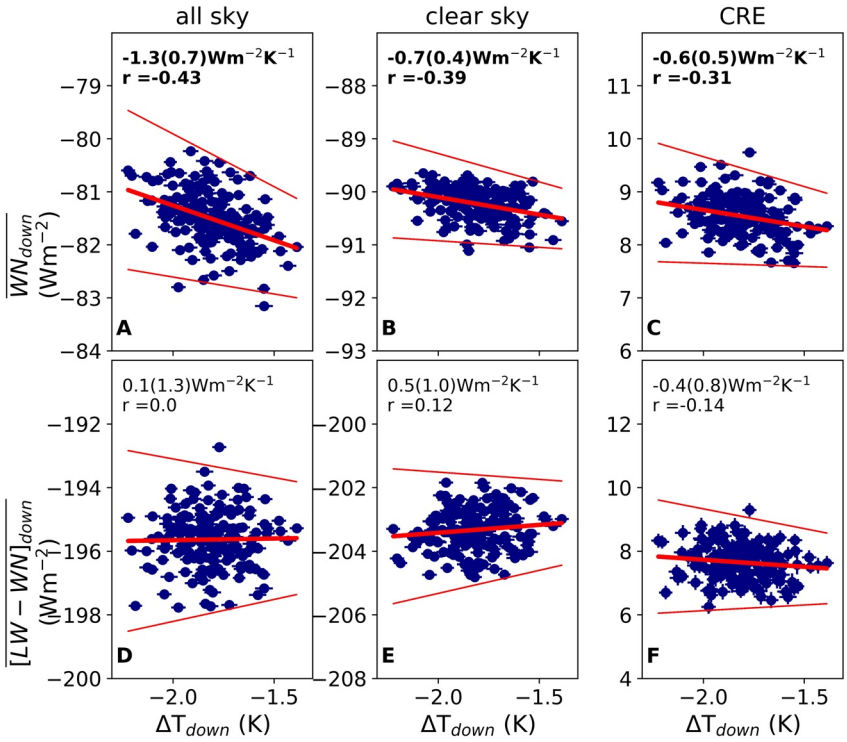

Figure 9. As Figure 6 but for descending regions.

shortwave radiation flux at the TOA: a warming effect. This effect of contrasting atmospheric responses to patterns in SST warming depending on relative warming in areas characterized by strong ascent or descent has been linked to climate sensitivity (Ceppi & Gregory, 2017).

Our results are robust against uncertainty due to the observational data coverage. Our use of large spatial scales and monthly means minimizes the impacts of missing clear-sky data on our conclusions. The independent, co-located CERES and AIRS data show a consistent picture, adding weight to our analysis, and there is also general agreement in behavior with ERA-I for the atmospheric data (Figures S1 and S2), and AIRS OLR all-sky and clear-sky radiation fluxes (Figure S3). While systematic biases in the AIRS data may affect the magnitude of the correlations shown here, our key conclusions are unlikely to be affected. We also test the impact of variations in solar zenith angles in the selected regions, by examining the proportion of incoming solar radiation reflected at the TOA, and find that this does not affect our conclusions (Figure S4). The nature of sun-synchronous data allows us to sample only part of the diurnal cycle, though general agreement with daily averages from ERA-I again suggests our results are robust against this. Another question is the sensitivity to the choice of median for defining regions of strong ascent and descent: we argue that a broad selection criterion is appropriate to select a coherent geographical region to reduce noise and focus on robust, large-scale relationships which may be of use for comparison to GCM output. However, we find that our conclusions also hold when the regions of strong ascent and descent are defined using the top 10th percentile of vertical velocity, though the effects are generally enhanced (Figures S5–S7). Our use of monthly mean vertical motion may include days of compensatory negative and positive motion, but studying large-area spatial means will mitigate against this. Furthermore, the distributions of strongly ascending and descending regions are broadly as we expect.

Our study has been primarily focused on the local effects of relative warming: how warming in ascending/descending regions affects atmospheric temperature and humidity, clouds, and radiative properties in the regions themselves. However, many previous modeling studies draw particular attention to the effects of warming in ascending areas on free-tropospheric temperature and humidity, and the subsequent effect on subsiding region stability and low cloud cover (Andrews & Webb, 2018; Zhou et al., 2017), which we only briefly examine here and for which some large scale observational evidence has been previously demonstrated

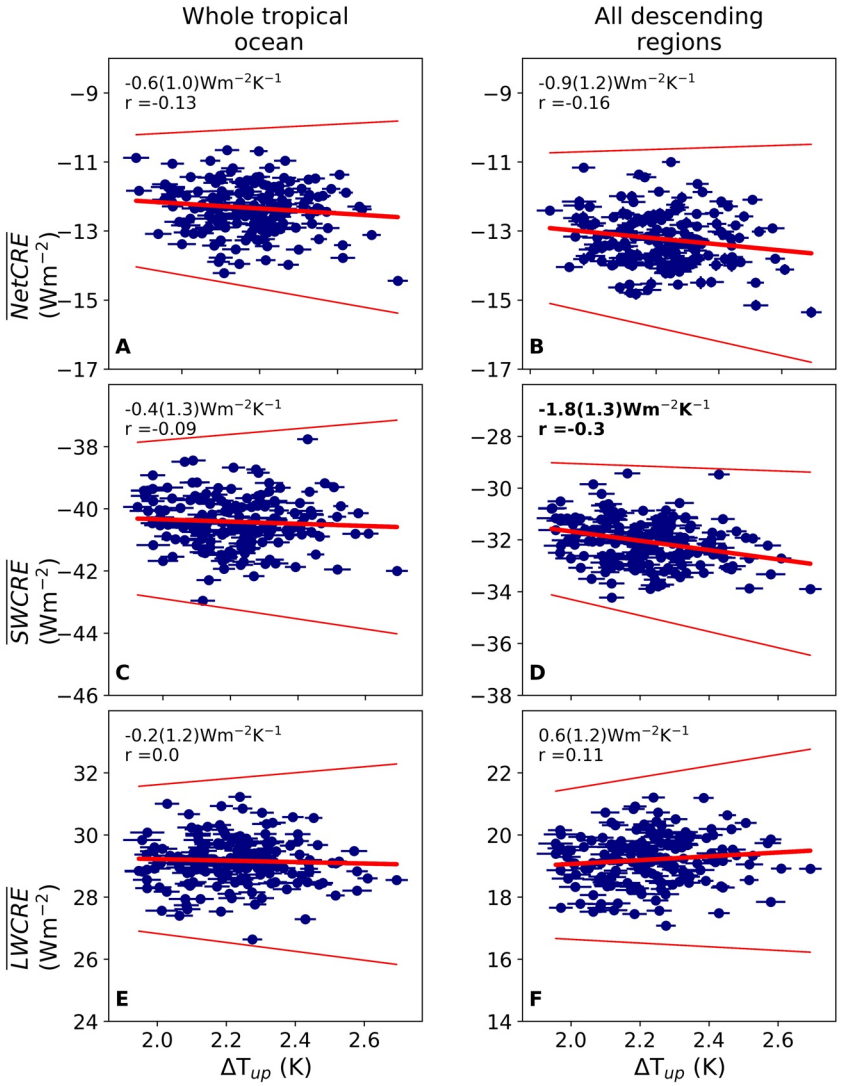

Figure 10. Scatterpots of ΔT_{up} and top-of-atmosphere cloud radiative effect (CRE) (defined as all-sky - clear-sky broadband radiation fluxes) over the whole tropical ocean (left column) and over all tropical regions of descent (right column, defined as any tropical ocean point with descending vertical velocity at 500 hPa in a given month). The CREs are split between (rows) net (shortwave and longwave) CRE, shortwave CRE (SWCRE), and longwave CRE (LWCRE). All data have been deseasonalized. A significantly outlying point has been removed. Radiation flux data are from CERES SSF1deg and SST data are from AIRS (see Section 2.2). The least squares linear fit is shown as a bold red line, with the associated error (three standard deviations) show as thin red lines. Inset text reports the fitted regression slope, with uncertainty (three standard deviations) in round brackets, and the Pearson correlation coefficient *r*. Text is bold if they are statistically significant ($p < 0.003$).

(Fueglistaler, 2019). The complete separation of local and nonlocal effects of SST warming patterns using observations is nontrivial: first, as they are calculated relative to the whole tropical ocean mean, $\overline{T_{trp}}$ (see Section 2.2), variations in both ΔT_{up} and ΔT_{down} may be affected by variations in $\overline{T_{trp}}$ as well as local warming or cooling; second, the atmospheric responses of the regions may be also be influenced by remote effects rather than solely changes in local SST. We address the former of these by testing the sensitivity of our results to selecting solely the points at month i which satisfy the condition $\mid \overline{T_{trp,i}} - \overline{T_{trp,i-1}} \mid < \mid \overline{T_{up/down,i}} - \overline{T_{up/down,i-1}} \mid$, namely those where the largest influence in the change in $\Delta T_{up/down}$ from the previous month is the mean temperature of the selected region, rather than the whole tropical ocean change. Using this condition does not significantly alter our conclusions (Figures S8 and S9). This, as well as the lack of correlation between $\Delta T_{up/down}$ and $\overline{T_{trp}}$ discussed in Section 2.2, increases our confidence that $\Delta T_{up/down}$ are not unduly influenced

by variations in $\overline{T_{trp}}$. The extent to which the ascending and descending atmospheric regions may be influenced by nonlocal SST variations is harder to quantify, indeed we find evidence that increases in ΔT_{up} are linked to changes in shortwave CRE in subsiding regions (Figure 10b, 10d, and 10f). However, our work here contains an implicit assumption that the predominant influence on local atmospheric response is the local SST. While our results are broadly consistent with model-based hypothesis described here, testing this assumption would be an interesting avenue for future modeling work.

A further avenue for future work is suggested by Figure 10 which shows that the effects of ΔT_{up} and ΔT_{down} on the mean tropical ocean radiation budget are not detectable on a monthly mean timescale: it would be of interest to examine at which timescales and lags, if any, SST of the warmest parts of the tropical ocean may modulate the tropical radiation budget. Linked to this is the question of prolonged warming: Zhou et al. (2016) link the dampened warming between the 1980s and 2000s to the relative warming of convective regions. Analysis over a longer time period may provide insight on how prolonged warming may affect the TOA radiation response. An interesting question would be to explore whether temperature, humidity, and cloud changes in ascending or descending regions are uniform, or whether there are spatial patterns which could be linked, for example, to monsoon systems. Further characterization of this could include the dependence of relative changes in these variables on the mean atmospheric state in different regions.

Our study examines observational evidence for proposed effects which have been linked to climate sensitivity. While our study largely supports the hypothesized mechanism of Andrews and Webb (2018) and others, as discussed, there are some notable aspects which remain unexplored. It would be of interest to know to what extent GCMs are able to reproduce the quantitative relationships using the same analysis method we use here. Recent work (Loeb et al., 2020) has shown that seven GCMs submitted to CMIP6 are able to track anomalies in observed TOA radiation fluxes over the last decades when forced with observed SSTs. However, they do not show the observed sensitivity to SST warming in the East Pacific, suggesting they are not sensitive enough to SST warming patterns. Closer examination of the processes governing the coupling between the lower and upper troposphere under different SST warming pattern scenarios in GCMs may shed light on contrasting behavior.

Data Availability Statement

CERES SSF1deg data were obtained from the NASA Langley Research Center Atmospheric Science Data Center (https://ceres.larc.nasa.gov/data/). AIRS data were obtained from (https://disc.gsfc.nasa.gov/datasets?page=1&source=AQUA%20AIRS&keywords=airs%20version%206).

Acknowledgments
AM was funded by a NERC doctoral training partnership grant (NE/L002558/1). This study was funded as part of NERC's support of the National Center for Earth Observation: HB and PIP were supported by grant number NE/R016518/1. We thank Paulo Ceppi and Michael Byrne for the helpful discussions.

References

Allan, R. P., Shine, K. P., Slingo, A., & Pamment, J. A. (1999). The dependence of clear-sky outgoing long-wave radiation on surface temperature and relative humidity. *Quarterly Journal of the Royal Meteorological Society*, *125*(558), 2103–2126. https://doi.org/10.1002/qj.49712555809

Andrews, T., Gregory, J. M., & Webb, M. J. (2015). The dependence of radiative forcing and feedback on evolving patterns of surface temperature change in climate models. *Journal of Climate*, *28*(4), 1630–1648. https://doi.org/10.1175/JCLI-D-14-00545.1

Andrews, T., Gregory, J. M., Webb, M. J., & Taylor, K. E. (2012). Forcing, feedbacks and climate sensitivity in CMIP5 coupled atmosphere-ocean climate models. *Geophysical Research Letters*, *39*(9). https://doi.org/10.1029/2012GL051607

Andrews, T., & Webb, M. J. (2018). The dependence of global cloud and lapse rate feedbacks on the spatial structure of tropical Pacific warming. *Journal of Climate*, *31*(2), 641–654. https://doi.org/10.1175/JCLI-D-17-0087.1

Armour, K. C. (2017). Energy budget constraints on climate sensitivity in light of inconstant climate feedbacks. *Nature Climate Change*, *7*, 331–335. https://doi.org/10.1038/nclimate3278

Aumann, H. H., Chahine, M. T., Gautier, C., Goldberg, M. D., Kalnay, E., McMillin, L. M., et al. (2003). AIRS/AMSU/HSB on the aqua mission: Design, science objectives, data products, and processing systems. *IEEE Transactions on Geoscience and Remote Sensing*, *41*(2), 253–264. https://doi.org/10.1109/TGRS.2002.808356

Bloch-Johnson, J., Rugenstein, M., & Abbot, D. S. (2020). Spatial radiative feedbacks from internal variability using multiple regression. *Journal of Climate*, *33*(10), 4121–4140. https://doi.org/10.1175/jcli-d-19-0396.1

Bony, S., & Dufresne, J.-L. (2005). Marine boundary layer clouds at the heart of tropical cloud feedback uncertainties in climate models. *Geophysical Research Letters*, *32*(20). https://doi.org/10.1029/2005GL023851

Bony, S., Dufresne, J.-L., Le Treut, H., Morcrette, J.-J., & Senior, C. (2004). On dynamic and thermodynamic components of cloud changes. *Climate Dynamics*, *22*, 71–86. https://doi.org/10.1007/s00382-003-0369-6

Boucher, O., Randall, D., Artaxo, P., Bretherton, C., Feingold, G., Forster, P., et al. (2013). Chapter 7: Clouds and aerosols. Climate change 2013: The physical science basis. In *Contribution of working group I to the fifth assessment report of the intergovernmental panel on climate change*, 571–658. https://doi.org/10.1017/CBO9781107415324.016

Bretherton, C. S. (2015). Insights into low-latitude cloud feedbacks from high-resolution models. *Philosophical Transactions of the Royal Society A: Mathematical, Physical and Engineering Sciences*, *373*(2054), 20140415. https://doi.org/10.1098/rsta.2014.0415

Brient, F., & Schneider, T. (2016). Constraints on climate sensitivity from space-based measurements of low-cloud reflection. *Journal of Climate*, *29*(16), 5821–5835. https://doi.org/10.1175/JCLI-D-15-0897.1

Brindley, H. E., & Harries, J. E. (1998). The impact of far I.R. absorption on clear sky greenhouse forcing: Sensitivity studies at high spectral resolution. *Journal of Quantitative Spectroscopy and Radiative Transfer*, *60*(2), 151–180. https://doi.org/10.1016/s0022-4073(97)00152-0

Ceppi, P., & Gregory, J. M. (2017). Relationship of tropospheric stability to climate sensitivity and Earth's observed radiation budget. *Proceedings of the National Academy of Sciences*, *114*, 13126. https://doi.org/10.1073/pnas.1714308114

Chen, T., Rossow, W. B., & Zhang, Y. (2000). Radiative effects of cloud-type variations. *Journal of Climate*, *13*(1), 264–286. https://doi.org/10.1175/1520-0442(2000)013<0264:REOCTV>2.0.CO;2

Doelling, D. R., Loeb, N. G., Keyes, D. F., Nordeen, M. L., Morstad, D., Nguyen, C., et al. (2013). Geostationary enhanced temporal interpolation for CERES flux products. *Journal of Atmospheric and Oceanic Technology*, *30*(6), 1072–1090. https://doi.org/10.1175/JTECH-D-12-00136.1

Fasullo, J. T., & Trenberth, K. E. (2012). A less cloudy future: The role of subtropical subsidence in climate sensitivity. *Science*, *338*(6108), 792–794. https://doi.org/10.1126/science.1227465

Fueglistaler, S. (2019). Observational evidence for two modes of coupling between sea surface temperatures, tropospheric temperature profile, and shortwave cloud radiative effect in the tropics. *Geophysical Research Letters*, *46*(16), 9890–9898. https://doi.org/10.1029/2019gl083990

Hartmann, D. L., Ockert-Bell, M. E., & Michelsen, M. L. (1992). The effect of cloud type on Earth's energy balance: Global analysis. *Journal of Climate*, *5*(11), 1281–1304. https://doi.org/10.1175/1520-0442(1992)005<1281:TEOCTO>2.0.CO;2

Held, I. M., & Soden, B. J. (2000). Water vapor feedback and global warming. *Annual Review of Energy and the Environment*, *25*(1), 441–475. https://doi.org/10.1146/annurev.energy.25.1.441

Klein, S. A., Hall, A., Norris, J. R., & Pincus, R. (2017). Low-cloud feedbacks from cloud-controlling factors: A review. *Surveys in Geophysics*, *38*, 1307–1329. https://doi.org/10.1007/s10712-017-9433-3

Klein, S. A., & Hartmann, D. L. (1993). The seasonal cycle of low stratiform clouds. *Journal of Climate*, *6*(8), 1587–1606. https://doi.org/10.1175/1520-0442(1993)006<1587:TSCOLS>2.0.CO;2

Lindzen, R. S., Chou, M.-D., & Hou, A. Y. (2001). Does the Earth have an adaptive infrared Iris? *Bulletin of the American Meteorological Society*, *82*(3), 417–432. https://doi.org/10.1175/1520-0477(2001)082<0417:DTEHAA>2.3.CO;2

Loeb, N. G., Doelling, D. R., Wang, H., Su, W., Nguyen, C., Corbett, J. G., et al. (2018). Clouds and the Earth's radiant energy system (CERES) energy balanced and filled (EBAF) top-of-atmosphere (TOA) edition-4.0 data product. *Journal of Climate*, *31*(2), 895–918. https://doi.org/10.1175/JCLI-D-17-0208.1

Loeb, N. G., Wang, H., Allan, R. P., Andrews, T., Armour, K., Cole, J. N. S., & Wyser, K. (2020). New generation of climate models track recent unprecedented changes in Earth's radiation budget observed by CERES. *Geophysical Research Letters*, *47*(5). https://doi.org/10.1029/2019gl086705

Mauritsen, T. (2016). Clouds cooled the Earth. *Nature Geoscience*, *9*, 865–867. https://doi.org/10.1038/ngeo2838

Mauritsen, T., & Stevens, B. (2015). Missing iris effect as a possible cause of muted hydrological change and high climate sensitivity in models. *Nature Geoscience*, *8*, 346–351. https://doi.org/10.1038/ngeo2414

McCoy, D. T., Eastman, R., Hartmann, D. L., & Wood, R. (2017). The change in low cloud cover in a warmed climate inferred from AIRS, MODIS, and ERA-Interim. *Journal of Climate*, *30*(10), 3609–3620. https://doi.org/10.1175/JCLI-D-15-0734.1

Minnis, P., Sun-Mack, S., Young, D. F., Heck, P. W., Garber, D. P., Chen, Y., et al. (2011). CERES edition-2 cloud property retrievals using TRMM VIRS and Terra and Aqua MODIS data-part I: Algorithms. *IEEE Transactions on Geoscience and Remote Sensing*, *49*(11), 4374–4400. https://doi.org/10.1109/TGRS.2011.2144601

Myers, T. A., & Norris, J. R. (2016). Reducing the uncertainty in subtropical cloud feedback. *Geophysical Research Letters*, *43*(5), 2144–2148. https://doi.org/10.1002/2015gl067416

Pierrehumbert, R. T. (1995). Thermostats, radiator fins, and the local runaway greenhouse. *Journal of the Atmospheric Sciences*, *52*(10), 1784–1806. https://doi.org/10.1175/1520-0469(1995)052<1784:TRFATL>2.0.CO;2

Qu, X., Hall, A., Klein, S. A., & Caldwell, P. M. (2014). On the spread of changes in marine low cloud cover in climate model simulations of the 21st century. *Climate Dynamics*, *42*, 2603–2626. https://doi.org/10.1007/s00382-013-1945-z

Qu, X., Hall, A., Klein, S. A., & Caldwell, P. M. (2015). The strength of the tropical inversion and its response to climate change in 18 CMIP5 models. *Climate Dynamics*, *45*(1), 375–396. https://doi.org/10.1007/s00382-014-2441-9

Qu, X., Hall, A., Klein, S. A., & DeAngelis, A. M. (2015). Positive tropical marine low-cloud cover feedback inferred from cloud-controlling factors. *Geophysical Research Letters*, *42*(18), 7767–7775. https://doi.org/10.1002/2015GL065627

Ramanathan, V., & Collins, W. (1991). Thermodynamic regulation of ocean warming by cirrus clouds deduced from observations of the 1987 El Niño. *Nature*, 27–32. https://doi.org/10.1038/351027a0

Scott, R. C., Myers, T. A., Norris, J. R., Zelinka, M. D., Klein, S. A., Sun, M., & Doelling, D. R. (2020). Observed sensitivity of low-cloud radiative effects to meteorological perturbations over the global oceans. *Journal of Climate*, *33*(18), 7717–7734. https://doi.org/10.1175/jcli-d-19-1028.1

Sherwood, S. C., Bony, S., & Dufresne, J.-L. (2014). Spread in model climate sensitivity traced to atmospheric convective mixing. *Nature*, *505*, 37–42. https://doi.org/10.1038/nature12829

Sherwood, S. C., Webb, M. J., Annan, J. D., Armour, K. C., Forster, P. M., Hargreaves, J. C., et al. (2020). An assessment of Earth's climate sensitivity using multiple lines of evidence. *Reviews of Geophysics*, *58*(4), e2019RG000678. https://doi.org/10.1029/2019rg000678

Soden, B. J., & Bretherton, F. P. (1993). Upper tropospheric relative humidity from the GOES 6.7 μm channel: Method and climatology for July 1987. *Journal of Geophysical Research*: Atmospheres, *98*(D9), 16669–16688. https://doi.org/10.1029/93jd01283

Soden, B. J., & Held, I. M. (2006). An assessment of climate feedbacks in coupled ocean-atmosphere models. *Journal of Climate*, *19*(14), 3354–3360. https://doi.org/10.1175/JCLI3799.1

Stephens, G. L. (2005). Cloud feedbacks in the climate system: A critical review. *Journal of Climate*, *18*(2), 237–273. https://doi.org/10.1175/JCLI-3243.1

Susskind, J., Barnet, C. D., & Blaisdell, J. M. (2003). Retrieval of atmospheric and surface parameters from AIRS/AMSU/HSB data in the presence of clouds. *IEEE Transactions on Geoscience and Remote Sensing*, *41*(2), 390–409. https://doi.org/10.1109/TGRS.2002.808236

Trenberth, K. E., Fasullo, J. T., O'Dell, C., & Wong, T. (2010). Relationships between tropical sea surface temperature and top-of-atmosphere radiation. *Geophysical Research Letters*, *37*(3). https://doi.org/10.1029/2009gl042314

Vial, J., Dufresne, J.-L., & Bony, S. (2013). On the interpretation of inter-model spread in CMIP5 climate sensitivity estimates. *Climate Dynamics*, *41*(11), 3339–3362. https://doi.org/10.1007/s00382-013-1725-9

Wong, S., Fetzer, E. J., Schreier, M., Manipon, G., Fishbein, E. F., Kahn, B. H., et al. (2015). Cloud-induced uncertainties in AIRS and ECMWF temperature and specific humidity. *Journal of Geophysical Research: Atmospheres*, *120*(5), 1880–1901. https://doi.org/10.1002/2014JD022440

Wood, R. (2012). Stratocumulus clouds. *Monthly Weather Review*, *140*(8), 2373–2423. https://doi.org/10.1175/MWR-D-11-00121.1

Wood, R., & Bretherton, C. S. (2006). On the relationship between stratiform low cloud cover and lower-tropospheric stability. *Journal of Climate*, *19*(24), 6425–6432. https://doi.org/10.1175/JCLI3988.1

Zelinka, M. D., Myers, T. A., McCoy, D. T., Po-Chedley, S., Caldwell, P. M., Ceppi, P., et al. (2020). Causes of higher climate sensitivity in CMIP6 models. *Geophysical Research Letters*, *47*. https://doi.org/10.1029/2019GL085782

Zhou, C., Zelinka, M. D., & Klein, S. A. (2016). Impact of decadal cloud variations on the Earth's energy budget. *Nature Geoscience*, *9*, 871–874. https://doi.org/10.1038/ngeo2828

Zhou, C., Zelinka, M. D., & Klein, S. A. (2017). Analyzing the dependence of global cloud feedback on the spatial pattern of sea surface temperature change with a green's function approach. *Journal of Advances in Modeling Earth Systems*, *9*(5), 2174–2189. https://doi.org/10.1002/2017MS001096